



Activity and durability of Pt–Ni nanocage electrocatalysts in proton exchange membrane fuel cells



Xiong Peng^a, Shuai Zhao^a, Travis J. Omasta^a, Justin M. Roller^b, William E. Mustain^{a,*}

^a Department of Chemical and Biomolecular Engineering, University of Connecticut, 191 Auditorium Drive, Storrs, CT 06269, United States

^b FEI, 5350 NE Dawson Creek Drive Hillsboro Oregon 97124, United States

ARTICLE INFO

Article history:

Received 23 March 2016

Received in revised form 24 October 2016

Accepted 28 October 2016

Available online 3 November 2016

Keywords:

PEM fuel cell

Nanocage

Oxygen reduction

High performance

Stability

ABSTRACT

A Ni-rich Pt–Ni alloy was synthesized via a solvothermal method and transformed into platinum–nickel nanocage catalysts (PNCs) by applying a two-phase corrosion process. The catalysts were physically and electrochemically characterized by X-ray diffraction (XRD), X-ray photoelectron spectroscopy (XPS), transmission electron microscopy (TEM) and both cyclic and linear sweep voltammetry using a rotating disk electrode (RDE). During the RDE testing, the half-wave potential of the PNC was 30 mV higher compared to that of a commercial Pt/C catalyst for the oxygen reduction reaction (ORR). The RDE experiments showed that the specific and mass activity of the PNC was 2 and 4 times greater than Pt/C, respectively, at 0.9 V. Catalyst-coated membranes (CCMs) were fabricated with the Pt–Ni nanocages using an automated air-assisted cylindrical liquid jet sprayer system. The PNC CCMs were loaded into proton exchange membrane fuel cells (PEMFC) for activity and stability testing. The CCMs showed no obvious Pt and Ni dissolution and redeposition in the membrane even after 30 K cycles. The performance and electrochemically active surface area (ECSA) retention of the PNC was far superior to commercial Pt/C, just short of the US Department of Energy (DOE) 2020 targets, suggesting that Pt–alloy nanocages are very promising candidates for high-performing commercial PEMFCs.

© 2016 Elsevier B.V. All rights reserved.

1. Introduction

Proton exchange membrane fuel cells (PEMFCs) are one of the most promising alternatives to combustion engines as power sources for transportation because of their environmental friendliness and high efficiency [1–3]. One of the main obstacles in the widespread commercialization of PEMFCs is the high cost of noble metal-based electrocatalysts. Reducing the amount of noble metals used in PEMFCs and finding higher activity catalysts remains a significant issue for fuel cell researchers. Platinum group metal catalysts remain the leading choices for the oxygen reduction reaction (ORR) and hydrogen oxidation reaction (HOR) [4]. However, since oxygen reduction is kinetically sluggish and 2–5 nm particles are inherently unstable, simple platinum and Pt–alloy nanoparticles may not be able to meet the 2020 DOE catalyst targets for PEMFCs [5,6], particularly for the ORR cathode.

In recent years, various approaches have been taken to develop higher activity electrocatalysts for the ORR. For example, controlling facets for single crystal Pt electrodes via surface atom

rearrangement can tune its catalytic performance [7] due to the structure sensitivity of the ORR on Pt low-index single-crystal surfaces [8]. In addition, developing Pt-based bimetallic and trimetallic electrocatalysts is said to increase ORR activity and stability several times over [9–11], which is attributed to a shift of d-band center on alloy surfaces [12]. More recently, Pt–M based (M = Co, Cu, Ni, et) cages have received research attention due to their three dimensional open structure that exposes more reacting sites by reducing the number of unutilized subsurface noble metal atoms [13–18]. Therefore, it is expected that Pt-based, cage-type electrocatalysts would show high ORR mass activity, and controlling their atomic-level structure can precisely and effectively tune their catalytic properties to achieve desirable activity and stability [19]. Recently, Stamenkovic and coworkers [20] demonstrated highly active rhombic dodecahedron Pt₃Ni nanocages with very good durability in ex-situ RDE experiments. They reported that the Pt₃Ni nanocage catalysts achieved a factor of 36 enhancement in mass activity and a factor of 22 enhancement in specific activity in RDE testing relative to a commercial Pt/C catalyst. They later reported some limited PEMFC data, where their Pt–Ni nanocages showed promising in-situ PEMFC performance [21]. However, they did not report durability data in an operating PEMFC or post-MEA charac-

* Corresponding Author.

E-mail address: mustain@engr.uconn.edu (W.E. Mustain).

terization, which are needed in order to understand how to design next-generation catalysts that exceed DOE targets.

Although these studies suggest that Pt-based nanocages are promising ORR catalysts, their data in an operating PEMFC is very limited and their in-situ activity and durability are poorly understood, which are essential to development of high performance, ultra low loading PEMFCs [22]. In this work, we first synthesized a Ni-rich Pt-Ni solid alloy using a modified solvent thermal synthesis method [10] and obtained Pt-Ni nanocages (PNCs) by applying a modified two-phase chemical corrosion method [15]. The activity and durability of the PNCs in operating PEMFCs, as well as the catalyst degradation impacts on fuel cell performance, were systematically studied before and after 30 K accelerated degradation cycles, which was essential to meet the 2020 DOE electrocatalyst targets for automotive PEM fuel cells [23].

2. Experimental section

2.1. Chemicals

Platinum(II) acetylacetone (98%, Fisher), Nickel(II)-acetylacetone (96%, Fisher), Ethylenediamine Tetraacetic Acid (Certified ACS), Disodium Salt Dihydrate (Certified, Fisher), PolyvinylPyrrolidone (PVP, Ave. F.W. 40,000, Fisher), Oleylamine (70%, Aldrich), Benzyl Alcohol (Certified, Fisher), Aniline (100% w/v, Fisher), Ethanol (Histological grade, Fisher), 2-Propanol (Optima, Fisher), Toluene (99.8%, Alfa Aesar), Cyclohexane (HPLC Grade, Fisher), Nafion ionomer dispersion (5% wt, DuPont), Perchloric acid (70% GFS), Gas diffusion layer (GDL, Sigracet 25BC), Pt/C catalyst (50%, TKK, Japan), NafionTM Membrane NR-212 (Ion Power).

2.2. Catalyst preparation

In a typical synthesis of the Pt-Ni alloy, 400 mg of PVP was dissolved into 25 mL Benzyl alcohol and the mixture was sonicated for 10 min. 70 mg Pt(acac)₂, 60 mg Ni(acac)₂ and 7 μ L aniline were added into the transparent mixture followed by a 10-min sonication and stirring. The resulting homogenous solution was transferred to a 50 mL Teflon-lined autoclave. After an overnight heating at 170 °C, the autoclave was cooled down to room temperature with cold tap water. The resulting Pt-Ni alloy was washed with an ethanol-acetone (1:1 in volume) mixture three times and separated from the liquid phase via centrifugation at 8000 RPM. The Pt-Ni alloy was then dispersed into a mixture of 45 mL ethanol and 15 mL oleylamine followed by reflux with vigorous stirring in nitrogen atmosphere at 200 °C for 5 h. The oleylamine-capped Pt-Ni alloy was washed with an ethanol-toluene (1:1 in volume) mixture three times and precipitated via centrifugation at 8000 RPM. Then, the alloy was re-dispersed into 15 mL of toluene in a vial to which 21 μ L of oleylamine was added. The dispersion was split into two equal-volume samples. Each sample was transferred into a separate 50 mL Teflon-lined autoclave constituting the upper oil phase; whereas a bottom aqueous phase was prepared by a solution of 10 mL DI water and 80 mg EDTA-2Na. The autoclaves were well sealed and kept at 110 °C for 12 h and cooled down to room temperature. The resulting PNC were washed with an ethanol-cyclohexane (1:1 in volume) mixture three times. One typical synthesis can yield around 25 mg of the Pt-Ni nanocages (12.5 mg in each autoclave). Finally, the 25 mg of nanocages were dispersed in 20 mL ethanol for characterization and electrochemical measurements.

2.3. CCM preparation

25 mg of Vulcan carbon (XC-72) was added into the ethanol-dispersed PNC, making a 50wt% Pt-Ni cage/Vulcan (PNC) catalyst.

The mixture was sonicated and separated via centrifugation at 8000 RPM. The PNC catalyst was vacuum dried at 70 °C for 5 h, followed by thermal annealing at 300 °C for 3 h under flowing hydrogen atmosphere. The CCM was fabricated by preparing an ink of 13 mg of PNC supported by Vulcan carbon and 10 mL IPA with 160 mg Nafion dispersion through a home-made air-assisted cylindrical liquid jets spraying system (Fig. S1) and the spraying pattern was shown in Fig. S2. The CCM fabrication method and conditions are detailed in the Supporting information [24,25].

2.4. Characterization

X-ray diffraction (XRD) of the carbon-supported catalyst was performed using a Bruker XRD advance D8 on a quartz sample holder. Data was collected from 30° to 90°. CCM surface morphology and cross-section were imaged by a FEI Quanta FEG 250 scanning electron microscope (SEM). Energy-dispersive X-ray spectroscopy (EDS) (TEAMTM EDS Analysis System) and EDS mapping were used to estimate and visualize Ni and Pt dissolution into the membrane. X-ray photoelectron spectroscopy (XPS) was conducted using a Physical Electronic multiprobe with a Perkin-Elmer dual anode X-ray source and a Kratos AXIS-165 surface analysis system to determine the oxidation states of surface platinum and nickel, as well as the atomic ratio between platinum and nickel in the PNC. Transmission electron microscope (TEM) and Scanning Transmission Electron Microscope (STEM) images were acquired on an FEI 200 kV Metrios TEM equipped with ChemiSTEMTM technology (Schottky field emission gun with an X-FEG source and Super-XEDS package). TEM (FEI Tecnai T12) was also used to determine the morphology and to measure the particle size of the Pt-Ni nanocage catalyst before and after 30,000 voltage cycles. A small portion of the PNC catalyst after 30,000 voltage cycles was scraped off of the cathode side of the CCM and dispersed in ethanol. The TEM samples were prepared by dropping 15 μ L of the dispersion on the TEM grid and drying at room temperature for 2 h. Finally, the pore size distribution of the CCMs was determined by mercury intrusion porosimetry (MIP) using a Micromeritics' AutoPore IV 9500.

2.5. Electrochemical measurements

Electrochemical measurements were conducted on a thin film rotating disk electrode (RDE) in a custom three-electrode glass (Adams & Chittenden Scientific Glass) cell using a platinum mesh as the counter electrode and Hg/HgSO₄ as the reference electrode. The working electrode was prepared on a 6 mm glassy carbon disk electrode (Pine Research Instrumentation) by dropping 13 μ L of a catalyst ink with the following composition: 7.6 mg catalyst, 7.6 mL IPA, 2.4 mL DI water and 20 μ L 5% Nafion dispersion, and drying on an inverted rotator at 700 RPM at room temperature. The three-electrode cell was washed using 18.2 MΩ Millipore DI water and 0.1 M HClO₄ five times each before testing.

2.6. CCM testing

The CCMs were assembled in single cell hardware with 25 cm² active area, a triple channel serpentine cathode plate and double channel serpentine anode plate. Sigracet 25BC was used as the gas diffusion layer on both sides. The average thickness of the CCM was 70 μ m, the total thickness of the Teflon gasket was 305 μ m, and the total thickness of GDL was 470 μ m, which led to a pinch of 185 μ m, corresponding to 38% of the total MEA thickness. The cell performance was tested on a Scribner 850e fuel cell test station. The performance was tested under H₂/O₂ flow with stoichiometry of 2, cell temperature of 80 °C and anode/cathode temperatures of 75 °C/73 °C (81%/75% relative humidity) at 150 Kpa_(abs). In order to accelerate the catalyst degradation, the MEA was cycled from

0.6 V to 1.0 V at a scan rate of 50 mV/s for 30,000 cycles with 200/75 standard cubic cm per minute of H₂/N₂ at 80 °C under 100% relative humidity, atmospheric pressure for the anode/cathode [26]. Polarization curves were obtained before and after cycling. The electrochemically active surface area (ECSA) of the MEA was estimated by cyclic voltammetry from 0.15 V to 1.2 V at a scan rate of 20 mV/s at a cell temperature of 25 °C, 100% relative humidity, 100/100 standard cubic cm per minute of H₂/N₂, 101 Kpa_(abs) at the anode/cathode before and after cycling.

3. Results and discussion

3.1. Physical characterization

TEM images of nanoparticles at different synthesis stages (Pt–Ni alloy and PNC) are shown in Fig. 1a–d. The initial Pt–Ni solid alloy was comprised of homogeneously sized, well-faceted crystals with a predominance of octahedral structure, which was attributed to the stabilization effect of the capping reagent [27]. The particle size of the Pt–Ni alloy synthesized here was smaller than the PtNi₃ polyhedra in Stamenkovic's work, which was expected based on the selection of a different capping reagent. The initial Pt–Ni alloy was converted to PNC by selective Ni corrosion via a modified two-phase corrosion method [15], which was a faster, more harsh procedure than that used in the Stamenkovic and coworkers, leading to some morphology variation; however, they both possessed continuous Pt–Ni crystallites with a 3-D hollow structure. As shown in Fig. 1c–d, the PNC possessed an 8-edge uniform octahedral morphology with average diameter of 8–10 nm. The continuous lattice fringes (inset of Fig. 1c) indicate that a monocrystalline nature was obtained, with interplanar spacing of 0.221 nm corresponding to the {1 1 1} facet of a face-centered cubic (fcc) structure [15].

XRD patterns for the Pt–Ni alloy and PNC are shown in Fig. 1e. Both XRD patterns showed four main peaks located around 39°, 46°, 67° and 87°, which can be ascribed to the corresponding (111), (200), (220) and (222) Pt fcc reflections (JXPDS database #04-0802). For both the Pt–Ni alloy and PNC, a slight shift to higher 2θ was noted for all peaks, which is likely due to the contraction of the Pt lattice by the incorporation of Ni atoms, indicating the formation of a Pt–Ni bimetallic system [28]. There were no evident peaks that could be attributed to either elemental Ni or Pt, suggesting the formation of a Pt–Ni alloy; however, there were potential shouldering peaks contained in the main peaks of the Pt–Ni alloy XRD pattern, indicating that different levels of alloying may have been present within the Pt–Ni alloy. Following the leaching steps to form the PNC, there was no phase separation and the final state of the Pt–Ni cage showed the formation of a thermally stable state. The characteristic XRD peaks of the PNC were shifted slightly toward lower angles compared to the Pt–Ni alloy, caused by an increase in lattice spacing due to preferential loss of Ni during the corrosion process [29], and transition from the Ni-rich Pt–Ni alloy to a Pt-rich Pt–Ni cage hollow structure [20].

The compositions of the Pt–Ni alloy and Pt–Ni nanocage catalysts were examined by XPS. The compositional changes occurring during different synthesis steps can provide critical information about morphology changes to the electrocatalyst. The broad survey scan was conducted within binding energies from 1100 to 0 eV. The relative Pt:Ni atomic ratio in the Pt–Ni alloy was around 0.96 while it was around 3.1 for the PNC, which verified the transformation of the Ni-rich alloy to Pt-rich cages (Fig. S4). Because Ni atoms are more susceptible to oxidation than Pt atoms in the presence of dissolved oxygen, the high-resolution Ni2p spectra (Fig. 2a) could be deconvoluted into five doublets with 57.6% of Ni in an oxidized state, while the high-resolution of Pt4f spectra (Fig. 2b) could be deconvoluted into two doublets with 35.9% of Pt in an oxidized

state (Pt²⁺ 4f) in Pt–Ni alloy. The four Pt peaks at 71.0 eV, 73.78 eV, 74.3 eV and 76.65 eV corresponded to the binding energy of Pt 4f_{7/2}, Pt²⁺ 4f_{7/2}, Pt 4f_{5/2} and Pt²⁺ 4f_{5/2}, respectively. Oxidized Ni is easier to dissolve than Pt due to the formation of complexes between Ni and oleylamine ligands [30]. The high-resolution spectra of Ni in the PNC (Fig. 2c) could be deconvoluted into two doublets, Ni–Pt 2p and Ni²⁺ 2p, with 31.5% in the Ni²⁺ state. The high-resolution Pt spectra for the PNC (Fig. 2d) could also be deconvoluted into two doublets, with 81.2% of the Pt in the metallic state and 18.8% being oxidized (Pt²⁺ 4f). The four peaks at 71.24 eV, 74.02 eV, 74.66 eV and 77.35 eV of Pt corresponded to the binding energy of Pt 4f_{7/2}, Pt²⁺ 4f_{7/2}, Pt 4f_{5/2} and Pt²⁺ 4f_{5/2}, respectively. The portion of atoms in the metallic state with respect to both Ni and Pt increased significantly, implying the dissolution of oxidized metals during the corrosion process. It is also interesting to note that the Ni2p binding energy shifted to a lower value in the PNC compared with the Pt–Ni alloy, indicating a change in the surrounding environment of the Ni atoms, which might due to the formation of a Pt-rich structure after corrosion.

3.2. Ex-situ RDE characterization

Fig. S5 shows cyclic voltammograms (CVs) for both the PNC catalyst and Pt/C. The data was collected at room temperature in N₂ purged 0.1 M HClO₄ electrolyte at scan rate of 20 mV/s. The PNC CV shows a very similar response to Pt/C, including in the H_{upd} adsorption/desorption region and the formation of the OH_{ad} layer at higher potentials [31]. The electrochemically active surface area (ECSA) was determined by integrating the double layer corrected hydrogen adsorption charge in the negative scan and dividing by 210 μC/cm², which corresponds to the adsorption of a hydrogen monolayer on polycrystalline Pt. The ECSA of PNC (71.16 m²/g_{Pt}) was more than two times greater than Pt/C (32.2 m²/g_{Pt}), most likely because of the open cage structure, which does not waste as many Pt atoms in the catalyst bulk. Details for the ECSA calculation are available in the Supporting information.

ORR linear sweep voltammograms were collected in O₂-saturated 0.1 M HClO₄ at a scan rate of 10 mV/s from 0.05 V to 1.03 V at 1600 RPM at 25 °C. Each experiment was performed at least three times to ensure reproducibility at the same experimental conditions and the results are shown in Fig. 3a. The electrocatalytic response of the Pt–Ni alloy was very similar to the commercial Pt/C TKK catalyst; however, the PNC nanocage catalyst showed a significant increase in the ex-situ activity compared to Pt/C and the Pt–Ni alloy. In fact, the ORR half-wave potential (E_{1/2}) of the PNC catalyst was 30 mV more positive than that of the Pt–Ni alloy and Pt/C, indicating superior ORR activity [32]. To be more quantitative regarding the activity, the kinetic current at 0.9 V vs. NHE was calculated from the ORR polarization curve after correcting for mass transport [33]. The mass activity of the PNC catalyst was found to be 501 mA/mg_{Pt}, which was over four times greater than that of Pt/C (104 mA/mg_{Pt}). After normalization to the ECSA, the specific activity of the PNC (704 μA/cm²) was over two times higher than that of Pt/C (323 μA/cm²). The higher activity of PNC than Pt/C is likely stemming from a combination of high intrinsic activity enabled by the alloy shift in the d-band center as well as the open architecture of cages leading to improved access to reactive sites.

3.3. CCM morphology and PEMFC performance

The surface morphology of CCMs prepared with the PNC at as both the anode and cathode catalyst was examined by scanning electron microscopy (SEM). As shown in Fig. 4, the catalyst layer (CL) possessed a very porous architecture and uniform agglomerations of carbon particles due to the formation of a wide distribution

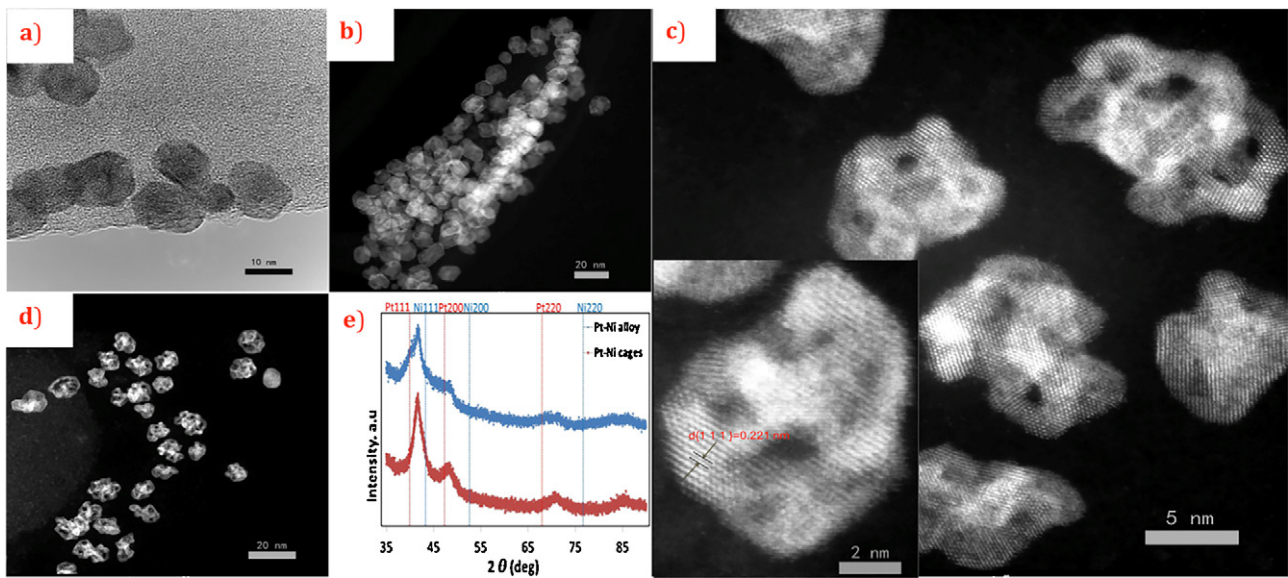


Fig. 1. Representative (a) (b) TEM images of the initial synthesized octahedral Pt-Ni alloy; (c) (d) TEM images of PNC at different resolutions; (e) XRD patterns of carbon-supported Pt-Ni alloy and PNC catalyst.

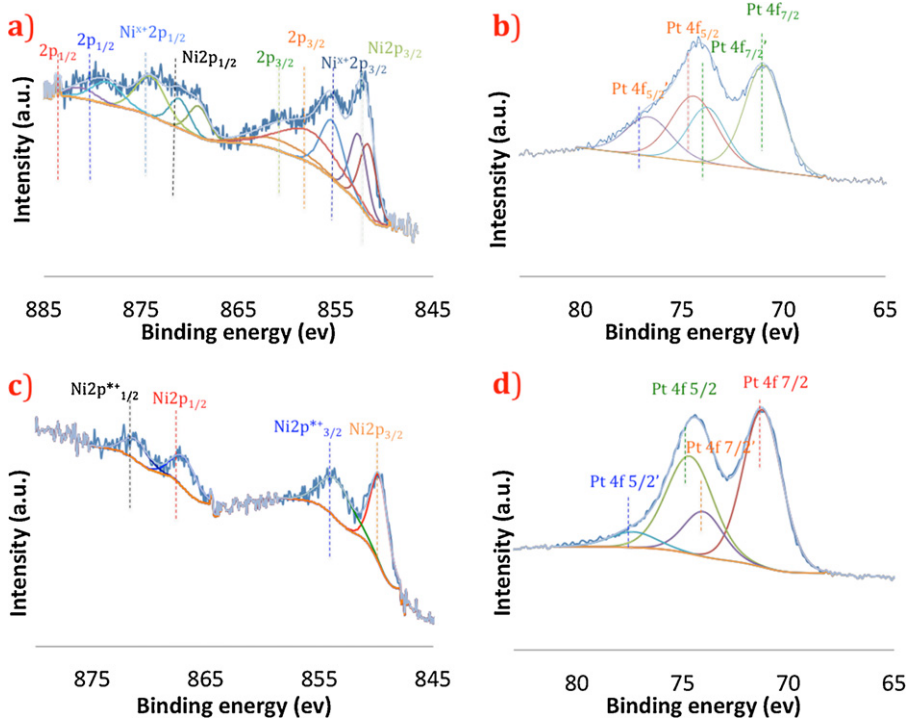


Fig. 2. High resolution (a) Ni 2p and (b) and Pt4f XPS spectra of the Ni-rich Pt-Ni alloy showing a highly oxidized surface; High resolution (c) Ni2p and (d) Pt4f XPS spectra of the Pt-Ni nanocages showing reduced surface oxidation and a slight shift in the Ni 2p binding energy after the controlled corrosion of the interior atoms.

of fragment sizes of the ink peeled off by fast gas stream during the spraying process [34], which is thought to be beneficial for water back diffusion and fuel mass transfer [25,35]. EDX and elemental mapping results are shown in Fig. S3, where it was observed that both platinum and nickel were evenly distributed throughout the studied area, indicating a uniform dispersion of catalyst on the membrane. Fig. S6 shows the pore-size distribution of both the PNC CCM and a Pt/C CCM. There were two main peaks for the CCMs: a smaller peak in the range of 3–10 nm and a larger peak in the range of 30–100 nm. The PNC CCM had a much larger mesopore volume (70–90 nm) than the Pt/C CCM. Though this may not be expected considering that the differences between the PNC and Pt/C catalysts

are observed on the nanoscale, there are two important considerations. First, the surface of the PNC is much more hydrophilic than Pt/C. Second, the PNC ink to create the CCM incorporated carbon black as an additive as opposed to a true support with catalyst bonded to the surface. Both of these will impact the formation of carbon agglomerates within the ink as well as impact the structure formation during solvent evaporation and drying. Finally, the pore size distribution also showed a significantly higher peak at ~3 nm than the Pt/C CCM, which might result from the 3-D hollow structure of the cages leading to a deeper penetration of Nafion into the cage and a higher ECSA.

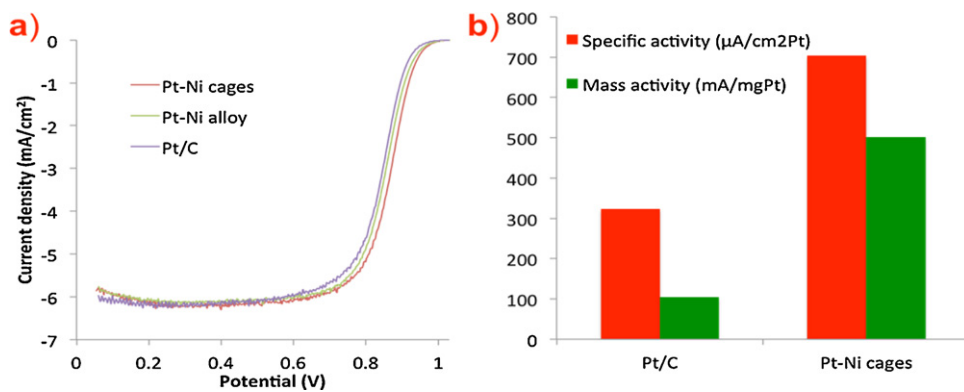


Fig. 3. (a) ORR polarization curves for Pt/C, Pt-Ni alloy and PNC showing considerably improved (b) specific activity and mass activity for Pt-Ni nanocage catalysts compared to state-of-the-art commercial Pt/C TKK catalyst.

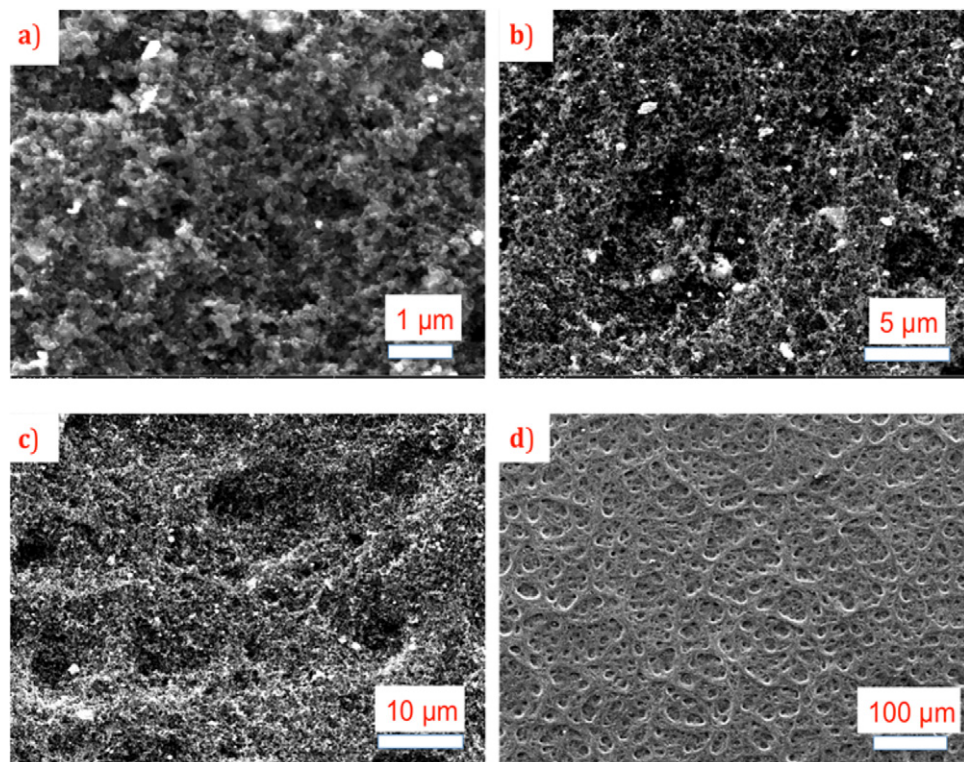


Fig. 4. SEM images of the cathode CL with Pt-Ni nanocages/Vulcan (PNC) catalyst under different magnifications. (a) and (b) show two magnified areas that clearly show the a pore architecture and homogeneous distribution of the carbon agglomerates and catalyst particles. (c) and (d) are lower magnification images that show that the CCM structure was homogenous and that there were no obvious cracks or mud-like morphologies formed during CL deposition.

PEMFC polarization curves of the CCMs with PNC and Pt/C catalysts are shown in Fig. 5a. The Pt/C PEMFC showed similar initial performance with lower loading compared to the literature [5]. Even though the PNC PEMFC ($0.1 \text{ mg}_{\text{Pt}}/\text{cm}^2$) had much lower platinum loading than that of Pt/C PEMFC ($0.3 \text{ mg}_{\text{Pt}}/\text{cm}^2$) on the cathode side, the PNC PEMFC polarization curve showed clearly superior performance than the Pt/C PEMFC. The mass-normalized current density (Fig. S7) of the PNC catalyst was significantly higher than Pt/C in both the kinetic (inset) and high current density regimes. In fact, at the typical operating point for PEMFCs, 0.7 V, the mass normalized current was more than 4 times higher for the PNC CCM than the Pt/C CCM. This higher PNC activity correlates exactly to the ORR kinetic data collected on the RDE. The higher PNC activity also resulted in a higher areal power density both at

the beginning of life ($1.28 \text{ W}/\text{cm}^2$ vs. $1.21 \text{ W}/\text{cm}^2$) and the end of life; this is despite the fact that the PNC CCM had only 1/3 the catalyst loading of the Pt/C CCM. In addition to the higher activity, the PNC CCM may have shown a higher peak power density than the Pt/C CCM because the catalyst layer was more porous, Fig. S6. In addition, the PNC catalyst showed very good stability, much better than Pt/C; the cell voltage was above 0.55 V even after 30 K cycles at current density of $1.9 \text{ A}/\text{cm}^2$. The mass activity loss for both PNC and Pt/C PEMFCs from the BOL to EOL is compared Fig. 5b. The PNC and Pt/C PEMFCs exhibited 58% and 81% mass activity loss at EOL after 30 K cycles, respectively, indicating that the PNC catalyst had a much better stability and was a large step closer to the 40% mass activity loss DOE 2020 [6]. Another important stability parameter is the in-situ ECSA, which was measured by cyclic voltammetry

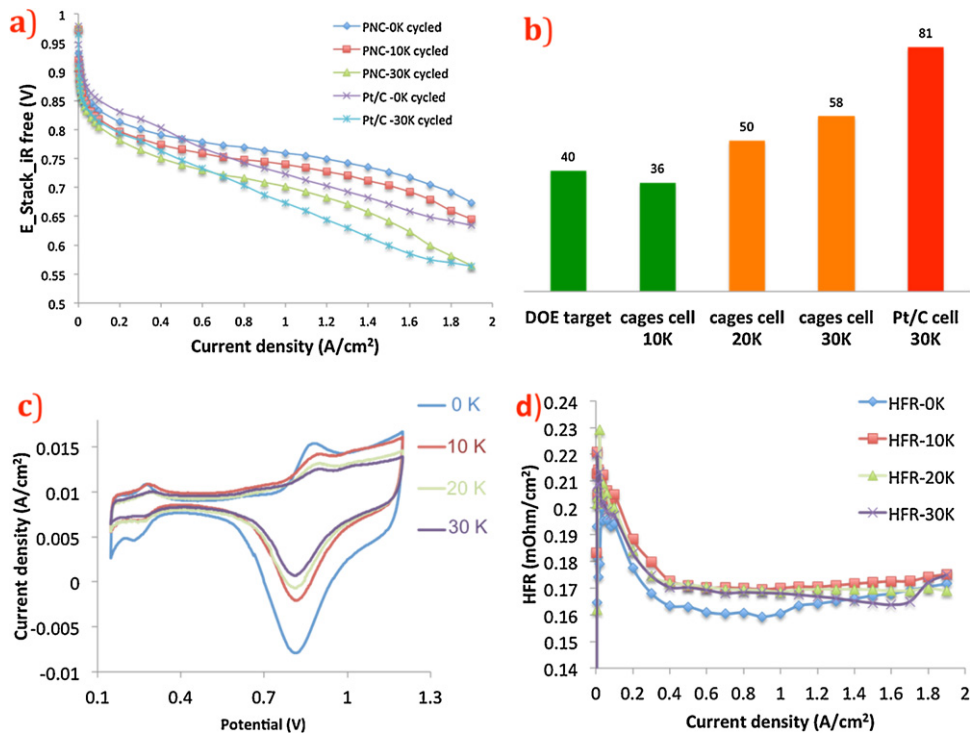


Fig. 5. (a) Polarization curves for PNC and Pt/C PEMFCs from BOL to EOL at different cycling stages; (b) Mass activity loss (%) of Pt-Ni nanocages and Pt/C during cycling, showing increased durability of the PNC catalyst vs Pt/C (obtained from the polarization curves at 0.9 V); (c) Cyclic voltammograms of the Pt-Ni nanocages PEMFC showing the ECSA losses during cell aging; (d) In-situ high frequency resistance (HFR) of the operating PEMFC with PNC catalyst.

[33]. The ECSA results for the PNC catalyst are shown in Fig. 5c. The ECSA of the PNC catalyst was reduced by 59% (from $42.4 \text{ m}^2 \text{ g}_{\text{Pt}}^{-1}$ to $17.2 \text{ m}^2 \text{ g}_{\text{Pt}}^{-1}$) after 30 K cycles. Interestingly, the reduction in the PNC mass activity and ECSA were near mirrors of one another, suggesting that the specific activity did not significantly reduce during testing. The mass activity loss for the Pt/C catalyst was also driven by the ECSA loss (Fig. S9), which was much more severe than the PNC catalyst. For both catalysts, a considerable majority of the mass activity and ECSA loss occurred during the first 10,000 cycles, suggesting the initial catalyst rearrangement is the driving force behind reduced performance throughout the PEMFC life. The ECSA loss most likely stems from the agglomeration of catalyst and the disappearance of edges during fuel cell operation and voltammetry cycling. In addition, it is also possible that some carbon corrosion occurred, leading to catalyst detachment and/or dissolution during accelerated degradation testing, which accelerated ECSA loss and performance decrease.

With regards to catalyst and cell degradation, it has been reported that the catalyst layer and Nafion membrane are susceptible to contamination by cations due to their limited protonic sites, and occupation of protonic sites by foreign cations leads to reduced CL and membrane conductivity and higher ohmic losses [5]. In order to investigate the ohmic losses resulting from possible Ni^{2+} and/or Pt^{2+} contamination of protonic sites due to leaching or dissolution from the Pt-Ni nanocages, the in-situ high frequency resistance (HFR) of the PNC PEMFC was measured at different cycling stages during cell operation and normalized by the active area of the cell and the result is shown in Fig. 5d. The cell showed higher HFR at low current density due to dehydration of both the anode and cathode and showed an increase in the HFR at high current density, which might result from possible catalyst layer flooding due to a faster H_2O generation rate at the cathode. However, the HFR did not show any significant change even after 30 K cycles, indicating few, if any,

protonic sites were occupied in the Nafion membrane area by Ni or Pt cations, which was also evidenced from elemental mapping of cross-section of CL before and after cycling, Fig. 6.

H_2 -crossover tests were conducted with increased aging of the PNC PEMFC and the result is shown in Fig. S10. In this test, the MEA was subjected to a linear sweep voltammetry test, which was performed in 100/100 sccm H_2/N_2 at 25 °C, 100% RH and 101 Kpa_{abs} at a scan rate of 2 mV/s from 0.1 V to 0.4 V. All of the H_2 oxidation current densities were mass transport limited with increasing electrode potential, which is indicative of a fuel cell with a very high electrical resistance without internal short [36]. The parasitic current density was around 0.38 mA/cm², indicating a nearly constant H_2 permeation rate from the anode side to the cathode before and after cycling [5]. The H_2 crossover data supports the HFR data, also suggesting that the PFSA membrane was not polluted by metal ions during the PEMFC operation and cycling [37,38].

Cross-sectional SEM images of the PNC CL before and after cycling are shown in Fig. 6a and e. The cross-section images show a thin CL with an even thickness of 9–10 micrometers, which is ideal for rapid gas supply and promoting the removal of water [39]. The CL was thinned after cycling, which may be caused by compression during cell assembly. Another possible explanation is collapse of the CL caused by degradation of both the catalyst and catalyst support during the long cycling process, which corresponded to the cell performance decrease that was observed after 30 K cycles. The EDS spectra and elemental mapping for the PNC CCM cross-section before and after 30 K cycles are shown in Fig. 6b–d and f–h, respectively. Both platinum and nickel showed a clear elemental boundary between the CL and membrane and a uniform distribution in the cross-section of the CL. It is also noted that even after 30 K cycles, there was no obvious Pt or Ni dissolution and re-deposition into the membrane, indicating a good stability of PNC, which also corresponded to the HFR results in Fig. 5d and the H_2 crossover

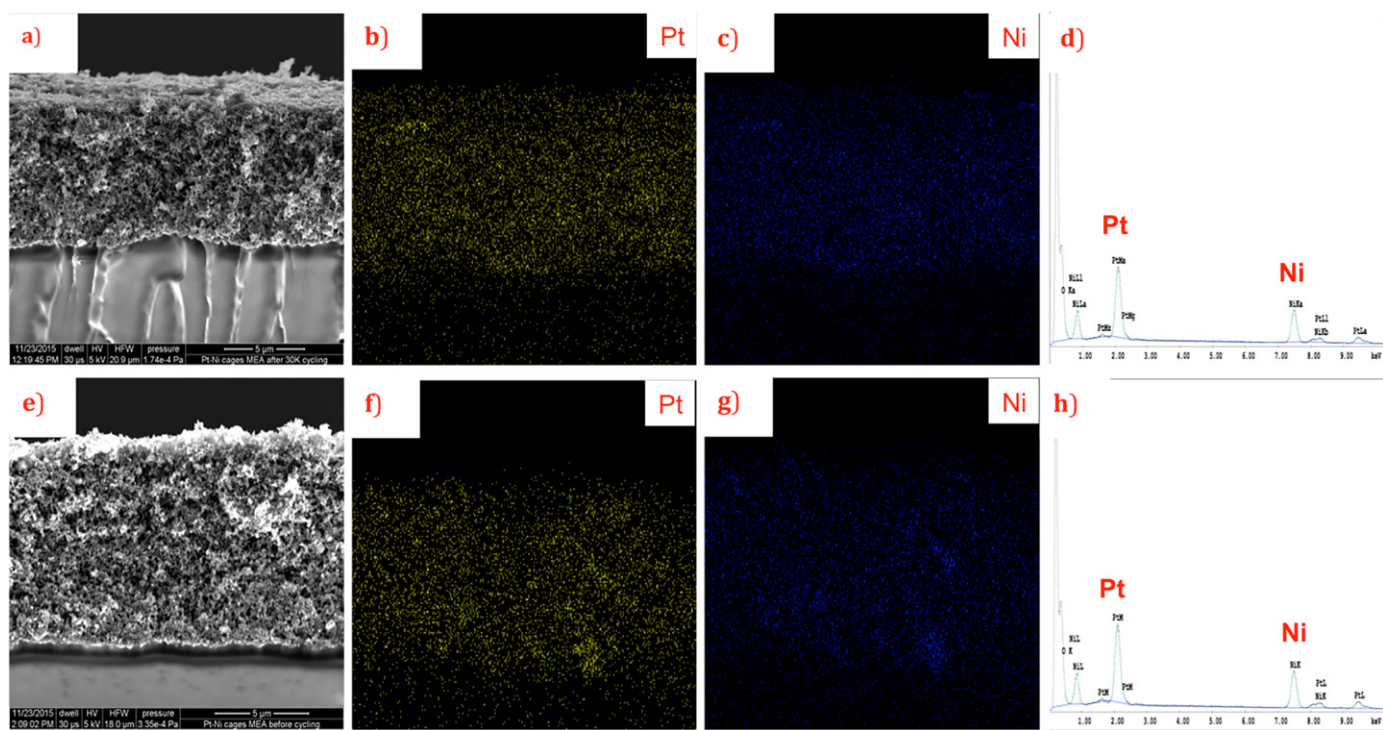


Fig. 6. (a) (d) SEM image and EDS spectra of CL cross-section before cycling; (b) (c) Pt and Ni elemental mapping of CL cross-section before cycling; (e) (h) SEM image and EDS spectra of CL cross-section after cycling; (f) (g) Pt and Ni elemental mapping of CL cross-section after cycling.

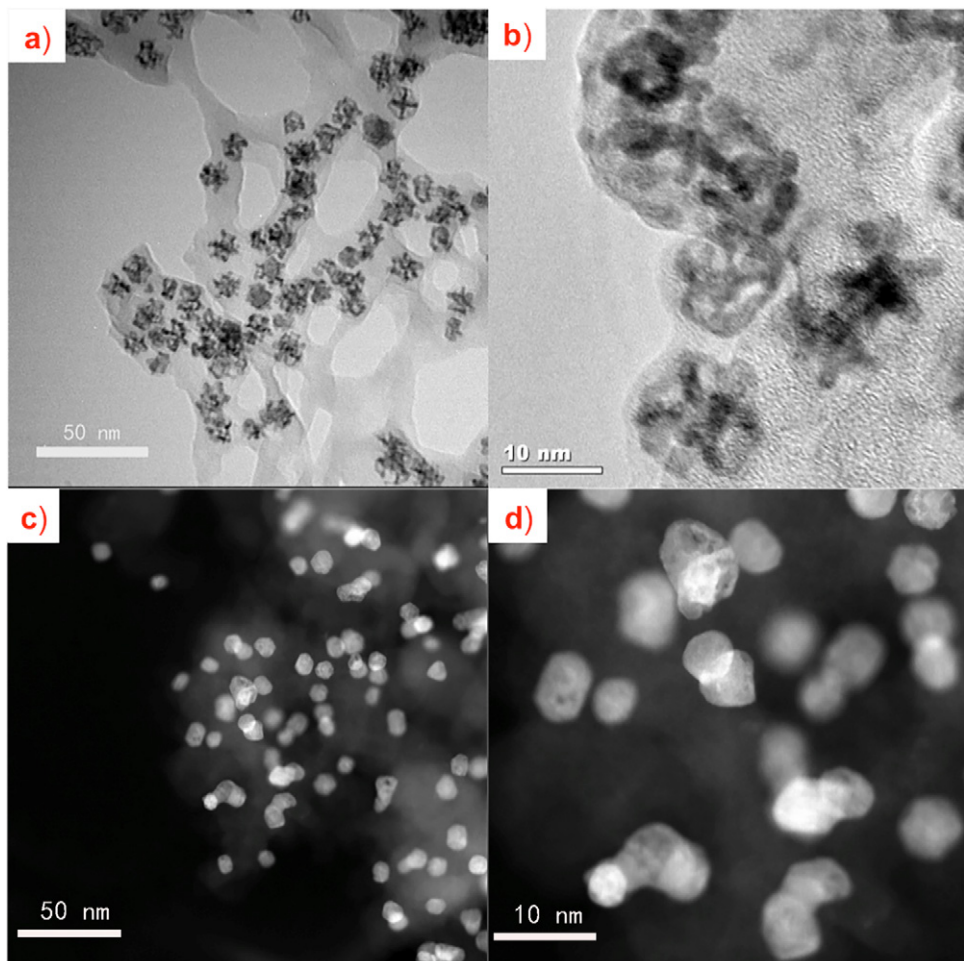


Fig. 7. (a) (b) TEM images of carbon-supported PNC before cycling; (c) (d) TEM images of carbon-supported PNC after 30 K cycling.

experiments. The Pt–Ni alloy CCM was also subjected to long-term testing followed by SEM and EDS elemental mapping for comparison (Fig. S11), and obvious Ni and Pt dissolution and re-deposition within the membrane area was observed.

TEM images of the PNC before and after 30 K cycles are shown in Fig. 7a–d. Samples were prepared by scratching materials from cathode side of MEA before and after cycling and placed on the TEM grid. The PNC showed a majority of cage structure before cycling (Fig. 7a–b). The PNC experienced slight agglomeration and some edge loss (Fig. 7c–d) after cycling. Some particles also became more spherical after fuel cell operation and 30 K degradation cycles due to surface energy loss while most of catalyst still retained 3-D hollow structure though with morphology transformation. The coalescence [40] and coarsening [41] of the PNC might be the root cause for mass activity and ECSA loss. However, an overwhelming majority of the particles retained their cage structure, showing that nanocage catalysts are chemically and structurally stable in operating PEMFCs.

4. Conclusions

In this work, Pt–Ni alloys and Pt–Ni nanocage electrocatalysts were successfully synthesized and characterized both physically and electrochemically (in-situ and ex-situ). In ex-situ RDE tests, the Pt–Ni nanoframe catalysts far outperformed commercial TKK Pt/C catalysts in terms of both specific and mass activity. The in-situ performance of the PNC was investigated in an operating 25 cm² PEMFC, and the MEA and catalyst degradation were studied after 30 K cycles. No Pt or Ni dissolution and redeposition into the membrane was found and the decrease of PEMFC performance mainly came from catalyst agglomeration and ECSA loss. Again, the Pt–Ni nanoframe catalysts significantly outperformed commercial Pt/C. The results highlight the superiority of PNC for both activity and durability in PEMFCs compared to existing carbon-supported Pt nanoparticles. The work presented here represent the first systematic study of activity and durability for PNC under PEMFC operation by using both physical and electrochemical methods that can be readily applied to multimetallic nanocage and other electrocatalysts.

Acknowledgements

This work was supported by the U.S. Department of Energy (DOE) award number DE-SC0010531. The author acknowledges the Institute of Materials Science and the Center for Clean Energy Engineering at the University of Connecticut for free use of the physical characterization equipment.

Appendix A. Supplementary data

Supplementary data associated with this article can be found, in the online version, at <http://dx.doi.org/10.1016/j.apcatb.2016.10.081>.

References

- [1] R.F. Service, FUEL CELLS: shrinking fuel cells promise power in your pocket, *Science* 296 (80–) (2002) 1222–1224.
- [2] S. CLEGHORN, Pem fuel cells for transportation and stationary power generation applications, *Int. J. Hydrogen Energy* 22 (1997) 1137–1144.
- [3] H. Zhang, P.K. Shen, Recent development of polymer electrolyte membranes for fuel cells, *Chem. Rev.* 112 (2012) 2780–2832.
- [4] NEWS OF THE WEEK Platinum in Fuel Cells Gets a Helping Hand, *Science* (80–). 315 (2007) 2007.
- [5] H.A. Gasteiger, S.S. Kocha, B. Sompalli, F.T. Wagner, Activity benchmarks and requirements for Pt-alloy, and non-Pt oxygen reduction catalysts for PEMFCs, *Appl. Catal. B Environ.* 56 (2005) 9–35.
- [6] (U.S. Department of Energy), Fuel Cell Technical Team Roadmap, Usdrive. (2013) 9.
- [7] Y. Nie, L. Li, Z. Wei, Recent advancements in Pt and Pt-free catalysts for oxygen reduction reaction, *Chem. Soc. Rev.* 44 (2015) 2168–2201.
- [8] V.R. Stamenkovic, B. Fowler, B.S. Mun, G. Wang, P.N. Ross, C. a Lucas, et al., Improved oxygen reduction activity on Pt3Ni(111) via increased surface site availability, *Science* 315 (80–) (2007) 493–497, <http://dx.doi.org/10.1126/science.1135941>.
- [9] Y. Jia, Y. Jiang, J. Zhang, L. Zhang, Q. Chen, Z. Xie, et al., Unique excavated rhombic dodecahedral PtCu 3 alloy nanocrystals constructed with ultrathin nanosheets of high-Energy {110} facets, *J. Am. Chem. Soc.* 136 (2014) 3748–3751.
- [10] Y. Wu, D. Wang, G. Zhou, R. Yu, C. Chen, Y. Li, Sophisticated construction of Au islands on Pt–Ni: an ideal trimetallic nanoframe catalyst, *J. Am. Chem. Soc.* 136 (2014) 11594–11597.
- [11] M.K. Carpenter, T.E. Moylan, R.S. Kukreja, M.H. Atwan, M.M. Tessema, Solvothermal synthesis of platinum alloy nanoparticles for oxygen reduction electrocatalysis, *J. Am. Chem. Soc.* 134 (2012) 8535–8542.
- [12] V.R. Stamenkovic, B.S. Mun, M. Arenz, K.J.J. Mayrhofer, C.A. Lucas, G. Wang, et al., Trends in electrocatalysis on extended and nanoscale Pt-bimetallic alloy surfaces, *Nat. Mater.* 6 (2007) 241–247.
- [13] G. Doubek, R.C. Sekol, J. Li, W. Ryu, F.S. Gittleson, S. Nejati, et al., Guided evolution of bulk metallic glass nanostructures: a platform for designing 3D electrocatalytic surfaces, *Adv. Mater.* (2016) 1940–1949.
- [14] L. Han, H. Liu, P. Cui, Z. Peng, S. Zhang, J. Yang, Alloy Cu3Pt nanoframes through the structure evolution in Cu–Pt nanoparticles with a core–shell construction, *Sci. Rep.* 4 (2014) 6414.
- [15] Y. Wang, Y. Chen, C. Nan, L. Li, D. Wang, Q. Peng, et al., Phase-transfer interface promoted corrosion from PtNi10 nanocuboctahedra to Pt4Ni nanoframes, *Nano Res.* 8 (2015) 140–155.
- [16] Z.-P. Zhang, W. Zhu, C.-H. Yan, Y.-W. Zhang, Selective synthesis of rhodium-based nanoframe catalysts by chemical etching of 3d metals, *Chem. Commun.* 51 (2015) 3997–4000.
- [17] P. Mani, R. Srivastava, P. Strasser, Dealloyed Pt – Cu core – shell nanoparticle electrocatalysts for use in PEM fuel cell cathodes, *J. Phys. Chem. C* 116 (40) (2012) 21334–21342.
- [18] K.C. Neyerlin, R. Srivastava, C. Yu, P. Strasser, Electrochemical activity and stability of dealloyed Pt Cu and Pt Cu Co electrocatalysts for the oxygen reduction reaction (ORR), *J. Power Sources*, 186, (2009) 261–267.
- [19] Y. Sha, T.H. Yu, B.V. Merinov, P. Shivanian, W.A. Goddard, Mechanism for Oxygen Reduction Reaction on Pt 3 Ni Alloy Fuel Cell Cathode, *J. Phys. Chem. C* 116 (40) (2012) 21334–21342.
- [20] C. Chen, Y. Kang, Z. Huo, Z. Zhu, W. Huang, H.L. Xin, et al., Highly crystalline multimetallic nanoframes with three-dimensional electrocatalytic surfaces, *Science* 343 (2014) 1339–1343.
- [21] N.M. Markovic, 2014 DOE Hydrogen and Fuel Cells Program Review Nanosegregated Cathode Catalysts with Ultra-Low Platinum Loading, Pls: Argonne National Laboratory Partners, 2014.
- [22] T. Roadmap, Hydrogen Storage Technologies Roadmap, Fuel Cell Technical Team Roadmap, 2013.
- [23] C. Wang, S. Wang, L. Peng, J. Zhang, Z. Shao, J. Huang, et al. Recent Progress on the Key Materials and Components for Proton Exchange Membrane Fuel Cells in Vehicle Applications, *Energies*, (2016), 9, 603.
- [24] C. Dumouchel, On the experimental investigation on primary atomization of liquid streams, *Exp. Fluids* (2008) 371–422.
- [25] I. Firtina, S. Güner, A. Albostan, Preparation and characterization of membrane electrode assembly (MEA) for PEMFC, *Int. J. Energy Res.* 35 (2011) 146–152.
- [26] N.L. Garland, Polymer DOE 's R & D Electrolyte Membrane Fuel Cell Catalyst Development Activities DOE 's Hydrogen & Fuel Cells Program addresses the key challenges, (2012) http://energy.gov/sites/prod/files/2014/03/f9/2.cwg-may2012_garland.pdf.
- [27] R. Narayanan, M. a El-Sayed, Effect of nanocatalysis in colloidal solution on the tetrahedral and cubic nanoparticle SHAPE: electron-Transfer reaction catalyzed by platinum nanoparticles, *J. Phys. Chem. B* 108 (2004) 5726–5733.
- [28] M.E. Scofield, C. Koenigsmann, L. Wang, H. Liu, S.S. Wong, Tailoring the composition of ultrathin, ternary alloy PtRuFe nanowires for the methanol oxidation reaction and formic acid oxidation reaction, *Energy Environ. Sci.* 8 (2015) 350–363.
- [29] Y. Wu, D. Wang, Z. Niu, P. Chen, G. Zhou, Y. Li, A strategy for designing a concave Pt–Ni alloy through controllable chemical etching, *Angew. Chemie Int. Ed.* 51 (2012) 12524–12528.
- [30] D. Wang, Y. Li, Effective octadecylamine system for nanocrystal synthesis, *Inorg. Chem.* 50 (2011) 5196–5202.
- [31] Y. Liu, W.E. Mustain, High stability, high activity Pt/ITO oxygen reduction electrocatalysts, *J. Am. Chem. Soc.* (2013) 2–5.
- [32] S. Guo, S. Zhang, S. Sun, Tuning nanoparticle catalysis for the oxygen reduction reaction, *Angew. Chemie, Int. Ed.* 52 (2013) 8526–8544.
- [33] Y. Garsany, O. a Baturina, K.E. Swider-Lyons, S.S. Kocha, Experimental methods for quantifying the activity of platinum electrocatalysts for the oxygen reduction reaction, *Anal. Chem.* 82 (2010) 6321–6328.
- [34] E. Villermaux, P. Marmottan, J. Duplat, Ligament-Mediated spray formation, *Phys. Rev. Lett.* 92 (2004) 074501.
- [35] J. Cao, M. Chen, J. Chen, S. Wang, Z. Zou, Z. Li, et al., Double microporous layer cathode for membrane electrode assembly of passive direct methanol fuel cells, *Int. J. Hydrogen Energy*. 35 (2010) 4622–4629.

- [36] K.R. Cooper, In situ PEMFC fuel crossover & electrical short circuit measurement, *Fuel Cell Mag.* (2008) 1–2 (Scribner A.I.).
- [37] R. Borup, J. Meyers, B. Pivovar, Y.S. Kim, R. Mukundan, N. Garland, et al., Scientific aspects of polymer electrolyte fuel cell durability and degradation, *Chem. Rev.* 107 (2007) 3904–3951.
- [38] A.C. Fernandes, E.A. Ticianelli, A performance and degradation study of Nafion 212 membrane for proton exchange membrane fuel cells, *J. Power Sources* 193 (2009) 547–554.
- [39] H.-K. Lee, J.-H. Park, D.-Y. Kim, T.-H. Lee, A study on the characteristics of the diffusion layer thickness and porosity of the PEMFC, *J. Power Sources* 131 (2004) 200–206.
- [40] C.E. Carlton, S. Chen, P.J. Ferreira, L.F. Allard, Y. Shao-Horn, Sub-Nanometer-Resolution elemental mapping of Pt 3 Co nanoparticle catalyst degradation in proton-Exchange membrane fuel cells, *J. Phys. Chem. Lett.* 3 (2012) 161–166.
- [41] E.F. Holby, W. Sheng, Y. Shao-Horn, D. Morgan, Pt nanoparticle stability in PEM fuel cells: influence of particle size distribution and crossover hydrogen, *Energy Environ. Sci.* 2 (2009) 865.